PAPER

Check for updates

Self-standing sulfur cathodes enabled by a single Fe site decorated fibrous membrane for durable lithium–sulfur batteries†

Gang Zhao,‡[a] Qiujie Chen,‡[bc] Lei Wang,[a] Tianran Yan,[a] Hongtai Li,[a] Cheng Yuan,[a] Jing Mao,[d] Xuefei Feng,[e] Dan Sun*[bc] and Liang Zhang [ID] *[a]

Rational design of sulfur host materials to synergize the retention and catalysis of lithium polysulfides (LiPSs) is of great significance to accomplish efficient sulfur electrochemistry for lithium–sulfur (Li–S) batteries. Herein, we have elaborately designed Fe single atom decorated porous carbon nanofibers (FeSA-PCNF) through electrospinning to construct self-standing and binder-free cathodes for Li–S batteries. The unique architecture of FeSA-PCNF with interconnected fibrous networks and hierarchical porous structures guarantees rapid charge transfer kinetics as well as abundant active interfaces for LiPS conversions. Moreover, the highly active FeN_4 moieties with surrounding graphitic N dopants embedded in the porous carbon nanofibers ensure strong chemisorption and superior electrocatalytic conversion towards LiPSs. As a consequence, the Li–S batteries assembled with FeSA-PCNF demonstrate superior electrochemical performances with a high rate capability of 791 mA h g^{-1} at 5C and a low capacity decay rate of 0.048% per cycle after 500 cycles at 2C. More encouragingly, a high areal capacity of 11.1 mA h cm^{-2} is achieved after 50 cycles with an ultrahigh sulfur loading of 17 mg cm^{-2} and a low electrolyte/sulfur ratio of 5 μl mg^{-1}. This work presents a promising strategy for rational design of self-standing and binder-free cathodes for practically feasible and high-performance Li–S batteries.

[a]*Institute of Functional Nano & Soft Materials (FUNSOM), Jiangsu Key Laboratory for Carbon-Based Functional Materials & Devices, Soochow University, 199 Ren'ai Road, Suzhou 215123, China. E-mail: liangzhang2019@suda.edu.cn*

[b]*CAS Key Laboratory of Design and Assembly of Functional Nanostructures, Fujian Key Laboratory of Nanomaterials, Fujian Institute of Research on the Structure of Matter, Chinese Academy of Sciences, Fuzhou, 350002 China. E-mail: xmsundan@fjirsm.ac.cn*

[c]*Xiamen Key Laboratory of Rare Earth Photoelectric Functional Materials, Xiamen Institute of Rare Earth Materials, Haixi Institutes, Chinese Academy of Sciences, Xiamen, 361021 China*

[d]*School of Materials Science and Engineering, Zhengzhou University, Zhengzhou 450001, China*

[e]*National Synchrotron Radiation Laboratory, University of Science and Technology of China, Hefei 230026, China*

† Electronic supplementary information (ESI) available. See https://doi.org/10.1039/d2ta01936a

‡ These two authors contributed equally to this work.

Dr Liang Zhang is a professor in the Institute of Functional Nano & Soft Materials (FONSOM) of Soochow University. He received his PhD degree in the application of synchrotron radiation from the University of Science and Technology of China under the direction of Prof. Junfa Zhu in 2013. He then got the Alexander-von-Humboldt fellowship and stayed at the University of Erlangen-Nuremberg under the supervision of Prof. Hans-Peter Steinrueck. From 2016 to 2018, he worked at the Advanced Light Source of Lawrence Berkeley National Laboratory as a postdoc fellow under the supervision of Dr Jinghua Guo. His research mainly focuses on the development of in situ/operando synchrotron radiation-based spectroscopy methods and their applications in energy storage materials.

This journal is © The Royal Society of Chemistry 2022

J. Mater. Chem. A, 2022, **10**, 19893–19902 | **19893**

Introduction

The ever-increasing energy demands of modern society have stimulated extensive exploitation of next generation high-energy-density and long-lifespan energy storage systems.[1,2] Lithium–sulfur (Li–S) batteries have been deemed as one of the most promising candidates owing to their high theoretical energy density (2600 W h kg^{-1}), environmental compatibility, and decent affordability.[3,4] Nonetheless, the practical applications of Li–S batteries have been plagued by several intractable challenges, including the insulating nature of sulfur and its lithiation products, huge volume variation ($\sim$80%) during cycling, the notorious shuttle effect of intermediate lithium polysulfides (LiPSs) and their sluggish conversion kinetics, which lead to inferior sulfur utilization and cycling stability.[5,6]

During the past few decades, various strategies have been proposed to solve the above-mentioned issues.[7–14] Among them, the rational design of advanced sulfur cathodes has been demonstrated to be an effective strategy to achieve high sulfur utilization and boost the battery performances.[15] It is worth noting that typical sulfur cathodes are fabricated by coating the mixture of active materials, host substrates and additives (e.g., carbon black and binders) onto the current collectors, in which the inactive components usually take up a large weight percentage of the cathodes and largely decrease the energy density of the Li–S batteries.[16] Moreover, the expansion stress during the sulfur redox process due to the mass density difference between sulfur and Li$_2$S can easily induce cracks or pulverizations in such conventional cathodes, especially under high sulfur loading conditions.[14] In this regard, it is highly desired to design self-standing sulfur cathodes with excellent conductivity, sufficient porosity, and structural integrity to improve Li–S electrochemistry especially under high sulfur loading conditions. Among various promising self-standing substrates candidates, electrospun carbon nanofibers with easily tailored structures and compositions have attracted significant attention.[17] The unique one-dimensional nanofibers enable fast electron conduction for sulfur redox reactions.[18] Moreover, high porosity inside the nanofibers can be easily achieved with the addition of pore formers, such as sacrificial polymers or metal–organic frameworks,[19–21] which can not only physically adsorb LiPSs but also buffer volume variations during cycling for enhanced electrode integrity.[18]

However, the pure physical adsorption of porous carbon nanofibers toward intermediate LiPSs only affords limited capability to suppress the shuttle effect, and the sluggish redox kinetics of LiPSs will inevitably lead to the accumulation of LiPSs in the electrolyte.[4] Accordingly, introducing catalysts with a strong chemisorption capacity and high electrocatalytic activity into the carbon substrates is a promising strategy to boost the electrochemical performances.[22] Recently, single-atom catalysts (SACs), which possess maximum atom utilization and unique electronic properties, have demonstrated great potential for Li–S batteries.[23] Notably, most reported SACs were prepared in the form of nanostructured powders, which were then fabricated as hybrid sulfur cathodes via the slurry-coating

method by mixing with additives and binders.[24–26] Such sulfur cathodes usually demonstrated infusive electrochemical performances mostly with a relatively low sulfur content. Therefore, it should be a promising strategy to couple SACs with electrospun carbon nanofibers to make full use of their synergistic effect for LiPS retention and catalysis of Li–S batteries under high sulfur loading conditions, which has been rarely reported so far.[22]

In this work, we have elaborately designed self-standing and binder-free sulfur cathodes with fibrous skeletons and porous structures by incorporating Fe single atoms into porous carbon nanofibers (FeSA-PCNF) to improve the electrochemical performances of Li–S batteries. During the synthesis process, Fe-doped zeolitic imidazolate frameworks (Fe-ZIF8) were first dispersed into the polymer solution followed by electrospinning, and then carbonized at high temperature to *in situ* form FeSA-PCNF with porous fiber skeleton structures. The interconnected fibrous networks with hierarchical porosity in the self-standing cathodes ensure efficient electrical charge transfer and buffer the volume variation during cycling, which leads to superb high-loading and rate performances of Li–S batteries. Meanwhile, the distensible surface area affords sufficient exposure of single Fe sites and abundant electrode/electrolyte interfaces for enhanced electrocatalytic activity. In addition, we also found that the N-rich polymer processor can offer additional graphitic N surrounding the FeN$_4$ moieties in FeSA-PCNF during the pyrolysis process,[27,28] which effectively increases the electron density of Fe atoms and thus further improves the activity of single Fe sites toward LiPS confinement and redox kinetics, as verified by experimental characterization studies and theoretical calculations. As a consequence, the Li–S batteries assembled with such self-standing and binder-free cathodes demonstrate a superior rate capability of 791 mA h g^{-1} at a high current density of 5C and a low capacity decay rate of 0.048% per cycle after 500 cycles at 2C. More impressively, a high areal capacity of 11.1 mA h cm^{-2} with an ultrahigh sulfur loading of 17 mg cm^{-2} and a low electrolyte/sulfur (E/S) ratio of 5 μl mg^{-1} is retained after 50 cycles. Our present study provides a promising strategy to construct self-standing sulfur cathodes for practically feasible, high-capacity, and long-lifespan Li–S batteries.

Results and discussion

The synthesis process of FeSA-PCNF is schematically depicted in Fig. 1a and the detailed synthesis procedure can be found in the Experimental section of the ESI†. In brief, Fe-ZIF8 nanocrystals with a diameter of approximately 100 nm (Fig. S1†) were first prepared following the procedures described in a previous work[29] and then dispersed into polyacrylonitrile (PAN) and poly(vinylpyrrolidone) (PVP) well-mixed solution for the following electrospinning process. Subsequently, the obtained fibrous membrane (Fig. S2†) was subjected to thermal pyrolysis to derive FeSA-PCNF (Fig. S3†). Note that the spontaneously evolved multilevel porosity originates from the evaporation of Zn species and the decomposition of low-carbon-yield PVP domains at elevated temperatures.[22,27] Meanwhile, the isolated
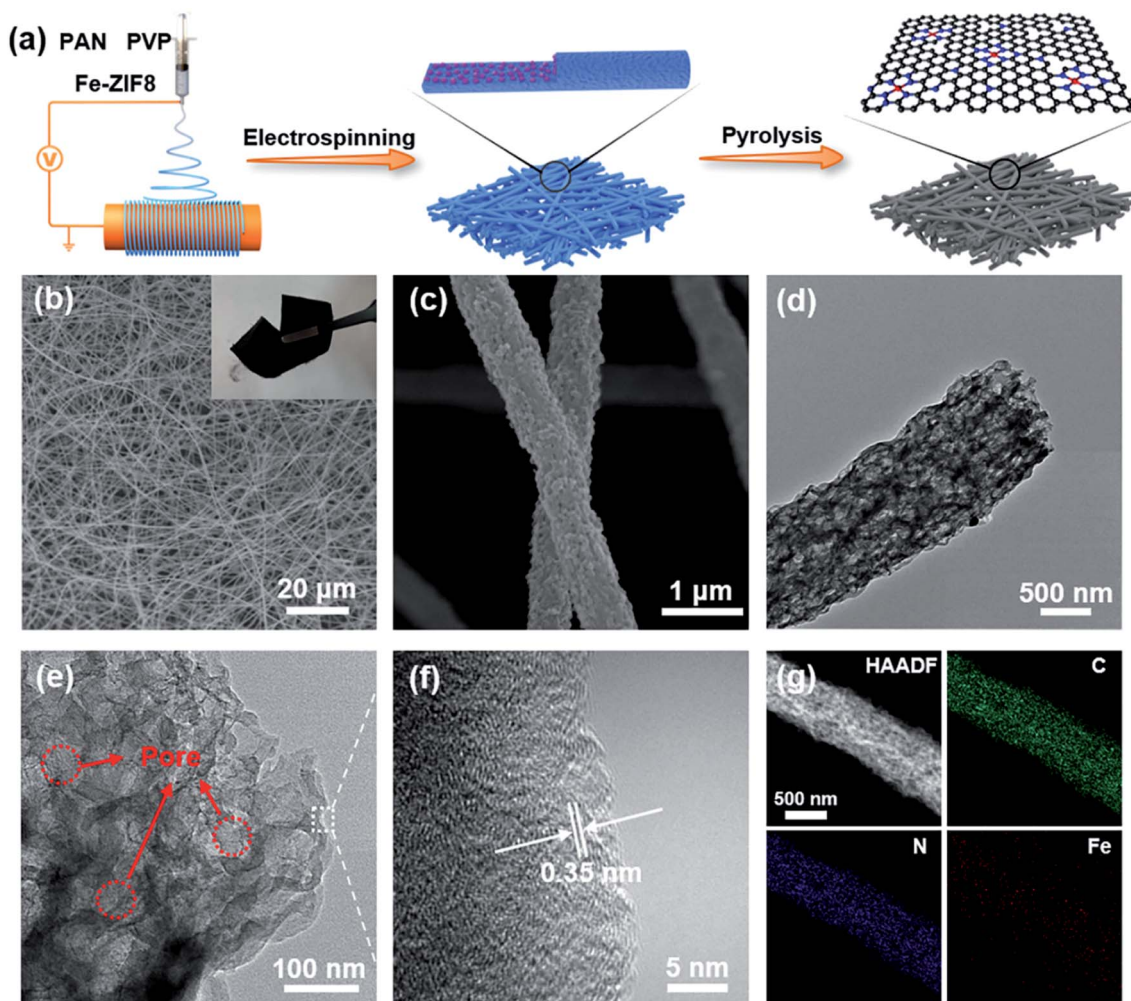
19894 | *J. Mater. Chem. A*, 2022, **10**, 19893–19902

This journal is © The Royal Society of Chemistry 2022

Fig. 1 (a) Schematic illustration of the preparation process of FeSA-PCNF. (b) and (c) SEM images of FeSA-PCNF. The inset of (b) shows the photograph of self-standing and flexible FeSA-PCNF. (d) and (e) TEM images of FeSA-PCNF. (f) HRTEM image of FeSA-PCNF. (g) Elemental mapping images of FeSA-PCNF.

Fe atoms coordinated with N atoms should be related to the *in situ* thermal pyrolysis of ZIF8 precursors. For comparison, porous carbon nanofibers (PCNF) (Fig. S4a†) prepared by substituting Fe-ZIF8 with bare zeolitic imidazolate frameworks (ZIF8) and a pure carbon nanofibers (CNF) (Fig. S4b†) prepared without ZIF8 were taken as reference samples *via* a similar protocol.

The morphological structures of FeSA-PCNF were characterized by scanning electron microscopy (SEM) and transmission electron microscopy (TEM). A 3D interconnected flexible network structure composed of randomly aligned carbon nanofibers is revealed for FeSA-PCNF (Fig. 1b and inset). The high-magnification SEM image (Fig. 1c) further shows the rough surface of porous carbon nanofibers with a diameter of ∼600 nm. A similar morphology is also observed for PCNF, while CNF demonstrate a smoother surface texture (Fig. S4b†). Moreover, the unique internal morphology of the nanofibers with distinct and well-distributed mesoporous and macroporous structures is well identified as shown in the TEM images (Fig. 1d and e). Such porous structures can facilitate the

exposure of single Fe sites and accommodate the huge volume change of sulfur species during cycling. The high-resolution TEM (HRTEM) image (Fig. 1f) manifests that FeSA-PCNF possess graphene-like layered structures with an interplanar distance of 3.5 Å, which assures rapid electron conductivity along the nanofibers. To corroborate the successful incorporation of Fe atoms into the nanofibers, elemental mapping characterization (Fig. 1g) was performed. The results reveal the uniform distribution of C, N, and Fe elements in FeSA-PCNF without any aggregation. In addition, the inductively coupled plasma-optical emission spectroscopy (ICP-OES) result (Table S1†) shows that the Fe content in FeSA-PCNF is 0.78 wt%.

The textural porosity of the three samples was further measured through N_2 adsorption–desorption isotherms (Fig. 2a and S5†). FeSA-PCNF show a typical type IV isotherm, similar to that of PCNF with a high specific surface area of 669.5 $m^2 g^{-1}$ and a pore volume of 0.96 $cm^3 g^{-1}$ (Table S2†). In contrast, CNF without ZIF8 demonstrate a type I isotherm with a smaller surface area of 228.9 $m^2 g^{-1}$ and a pore volume of 0.23 $cm^3 g^{-1}$ (Fig. S5 and Table S2†). The enlarged surface area is attributed
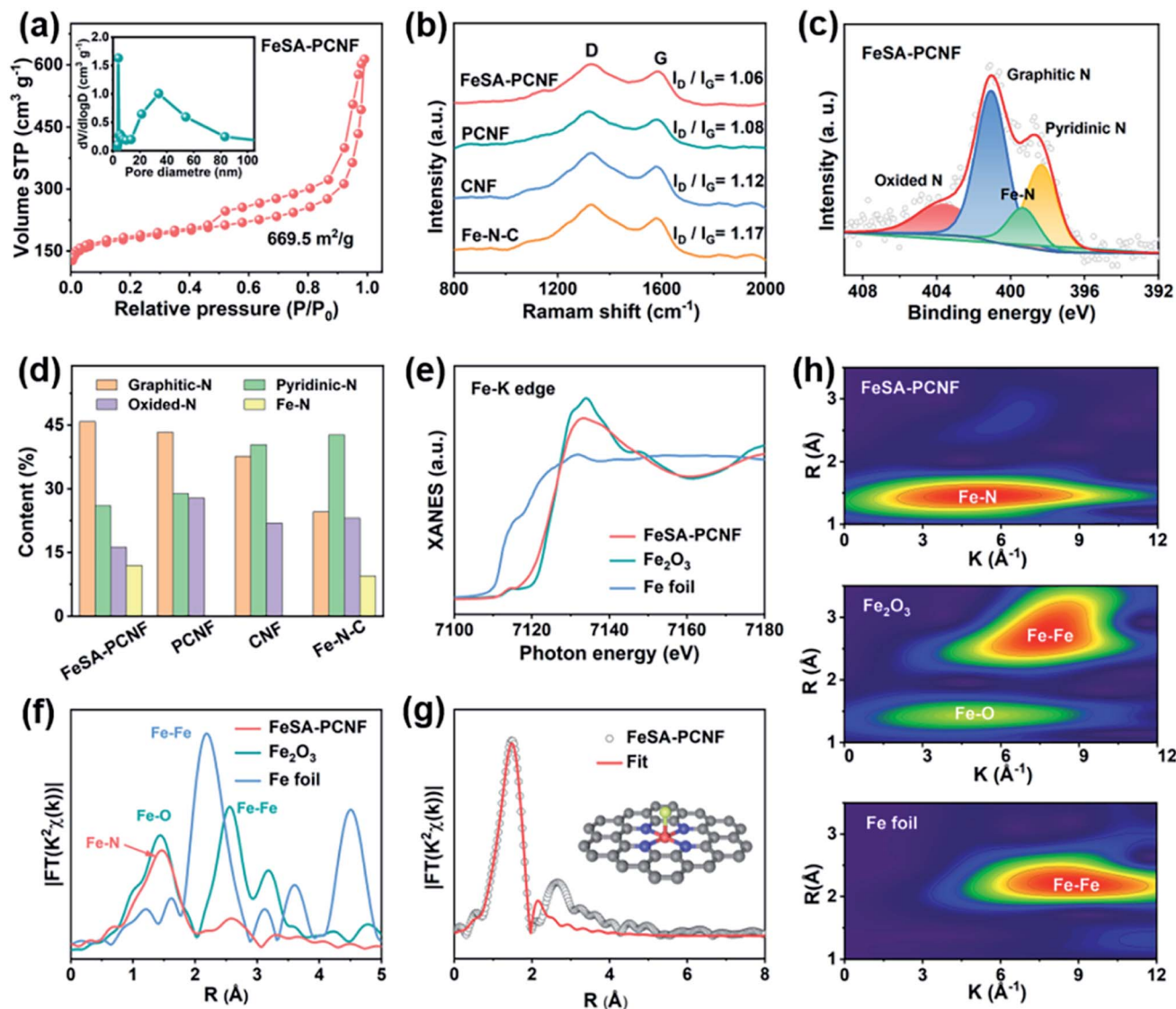
Fig. 2 (a) N_2 adsorption–desorption isotherms of FeSA-PCNF. The inset shows the corresponding pore size distribution curve. (b) Raman spectra of FeSA-PCNF, PCNF, CNF and Fe−N−C. (c) N 1s XPS of FeSA-PCNF. (d) The relative ratios of different N species in different samples. (e) Fe K-edge XANES spectra of FeSA-PCNF, Fe_2O_3, and Fe foil. (f) Fe K-edge FT-EXAFS spectra of different samples. (g) Fe K-edge FT-EXAFS spectra and the corresponding fitting curve of FeSA-PCNF. The inset shows the model of the proposed FeN_4 structure. The blue, gray, red, and green balls indicate N, C, Fe, and O atoms, respectively. (h) Wavelet transform plots of FeSA-PCNF, Fe_2O_3, and Fe foil.

to the evaporation of Zn species during pyrolysis, which facilitates the introduction of abundant cathode/electrolyte interfaces for efficient sulfur redox reactions.[18] Moreover, the high pore volume is promising to accommodate high sulfur loading and large volume variation upon cycling. The pore size distribution curve (inset of Fig. 2a) indicates that FeSA-PCNF exhibit hierarchical porous characteristics over a wide diameter range. The micropores in FeSA-PCNF are expected to offer strong physical confinement of LiPSs for restraining the shuttle effect[30] while the mesopores and macropores enable electrolyte infiltration and accessibility of inner single Fe sites buried under the carbon layers,[27] which can efficiently increase catalyst utilization. Raman spectroscopy was additionally performed to investigate the degree of graphitization of FeSA-PCNF (Fig. 2b).

Two prominent peaks located at 1337 cm^{-1} (D band) and 1587 cm^{-1} (G band) are observed. It has been revealed that the graphitization degree of carbon materials is closely related to the I_D/I_G ratio.[18,27] To figure out the influence of PAN and PVP polymers on single Fe sites, Fe−N−C prepared by direct pyrolysis of Fe-ZIF8 was also investigated. The results show that FeSA-PCNF have the lowest I_D/I_G ratio compared to PCNF, CNF, and Fe−N−C, which implies that FeSA-PCNF have the highest graphitization degree among the measured samples. The increased graphitization degree promises long-range and rapid electron transportation for fast sulfur redox reactions during cycling.[18]

X-ray photoelectron spectroscopy (XPS) was also utilized to analyze the different N species in the investigated materials. As

19896 | *J. Mater. Chem. A*, 2022, **10**, 19893–19902

This journal is © The Royal Society of Chemistry 2022

shown in Fig. 2c and S6,† the N 1s XPS spectra can be deconvoluted into four species, including pyridinic N at 398.5 eV, graphitic N at 401.2 eV, oxidized N at 403.5 eV, and N coordinated with Fe single atoms (denoted as Fe–N) at 399.5 eV. The different N dopants are expected to facilitate strong chemisorption of LiPSs by endowing the carbon substrates with polar surfaces, which can effectively suppress the shuttle effect and improve sulfur utilization.[18,31] Comparison of the ratios of different N species (Fig. 2d) shows that the ratio of graphitic N in FeSA-PCNF is higher than that of PCNF, CNF, and Fe–N–C. It is worth mentioning that the content of graphitic N could greatly influence the electrocatalytic activity of SACs, as reported previously.[27,28]

To investigate the chemical state and coordination environment of Fe sites in FeSA-PCNF, Fe K-edge X-ray absorption near-edge structure (XANES) and extended X-ray absorption fine structure (EXAFS) were measured. As shown in Fig. 2e, the near-edge absorption energy of FeSA-PCNF is close to that of Fe_2O_3 but higher than that of Fe foil, which implies that the Fe atoms are positively charged. The corresponding Fourier-transformed k^2-weighted EXAFS (FT-EXAFS) spectrum of FeSA-PCNF (Fig. 2f) only exhibits a main peak centered around 1.5 Å, which can be ascribed to Fe–N coordination. The absence of Fe–Fe coordination corroborates that the Fe atoms are atomically dispersed in FeSA-PCNF, which is consistent with the absence of Fe metal peaks in the XRD result (Fig. S7†). The quantitative least-squares FT-EXAFS fitting of FeSA-PCNF was subsequently performed (Fig. 2g), in which each Fe atom is coordinated by four N atoms and one O atom (Table S3†). These results further confirm the dominant Fe–N configuration in FeSA-PCNF. Note that the presence of coordinated O should be related to physically absorbed oxygen as a consequence of the high activity of single Fe atoms, as also observed in previous reports.[32] Furthermore, the wavelet transform (WT) of Fe K-edge EXAFS oscillations was performed owing to its cogent resolutions in both k and R spaces. The WT contour plot of FeSA-PCNF only displays one intensity maximum at 5 $Å^{-1}$, which can be ascribed to the Fe–N(O) coordination, in sharp contrast to that of Fe_2O_3 and Fe foil. Overall, the FT- and WT-EXAFS results clearly elucidate the single atom status of Fe in FeSA-PCNF.

To further evaluate the adsorption and electrocatalytic conversion capability of FeSA-PCNF for LiPSs, density functional theory (DFT) calculations were performed. According to the XPS results, graphitic N atoms are incorporated around the FeN_4 coordination structures of FeSA-PCNF. Therefore, different graphitic N substituting structures (marked as FeN_4, FeN_4–1N, and FeN_4–2N) were constructed to investigate the influence on the electronic structure and activity of FeSA-PCNF (Fig. S8†). For comparison, a pure N-doped carbon structure (denoted as CN_4) was also constructed and investigated. The adsorption energies of Li_2S_4 and Li_2S_6 on different surfaces (Fig. 3a and S9†) were calculated first. It is obvious that the adsorption energies of samples with single Fe sites are much higher than that of CN_4, indicating that single Fe sites can effectively confine LiPSs. However, the adsorption energies are slightly reduced after doping graphitic N in the neighboring carbon basal plane of FeSA-PCNF. Furthermore, the density of

states (DOS) calculation results indicate that graphitic N atoms could greatly influence the electronic configurations of single Fe sites of FeSA-PCNF (Fig. 3b). It can be clearly seen that the charge density of Fe atoms near the Fermi level is greatly enhanced, which could be related to the charge transfer from the neighboring electron-rich graphitic N to Fe centers, leading to the increased filling degree of d orbitals of Fe atoms.[33] The increased electron density of Fe d orbitals could slightly reduce the binding strength toward LiPSs but still at an acceptable level, while the electron transportation from FeSA-PCNF to LiPSs is greatly facilitated, which in turn accelerates the redox kinetics of LiPSs.[25,34] Therefore, the electrocatalytic activity of single Fe sites is further optimized by the introduction of neighboring graphitic N atoms into the carbon basal plane of FeSA-PCNF.

In order to visually verify the enhanced LiPS entrapment by FeSA-PCNF, an adsorption experiment and UV-vis absorption measurement were carried out (Fig. 3c). By immersing the same amount of FeSA-PCNF, PCNF, and CNF into the Li_2S_6 solution and allowing it to stand for the same time, it is shown that the solution with FeSA-PCNF becomes almost transparent. The UV-vis absorption spectra further show the largest reduction in peak intensity for FeSA-PCNF, indicating the strongest LiPS adsorption capability of FeSA-PCNF. XPS characterization was also employed to demonstrate the strong chemical interaction between LiPSs and FeSA-PCNF (Fig. 3d). The S 2p spectrum of Li_2S_6 exhibits two pairs of peaks centered at 161.7 and 163.2 eV, corresponding to terminal (S_T^{-1}) and bridging (S_B^0) sulfur, respectively. After interacting with FeSA-PCNF, the peaks shift largely to the high-energy direction, confirming the strong chemical affinity of FeSA-PCNF to LiPSs.

The above evidence strongly suggests that FeSA-PCNF are a promising candidate to both strongly confine LiPSs and accelerate LiPS redox kinetics. Symmetric cells were assembled with FeSA-PCNF, PCNF and CNF identical cathodes to investigate the redox kinetics of LiPSs. As shown in Fig. 3e, FeSA-PCNF demonstrate the highest redox current response at a scan rate of 10 mV s^{-1}, indicating faster and more favorable LiPS conversions. In the cyclic voltammetry (CV) curves with a scan rate of 1 mV s^{-1} (Fig. 3f), all cells exhibit two reduction peaks and one oxidation peak. The reduction peaks at approximately 2.33 and 2.05 V are respectively ascribed to the reaction producing soluble Li_2S_x ($4 \leq x \leq 8$) from sulfur and the subsequent reduction to Li_2S_2/Li_2S, while the oxidation peak at 2.3 V is assigned to the reverse reactions producing sulfur from Li_2S and Li_2S_2.[35] It is worth noting that FeSA-PCNF exhibit a higher reduction potential and a lower oxidation potential, indicating a smaller polarization. Moreover, the redox peaks of FeSA-PCNF are sharper and more compact compared to those of PCNF and CNF, which ensure boosted electrocatalytic activity and thus an effectively suppressed shuttle effect.

Ion diffusion is another vital parameter for LiPS redox reactions. CV measurement at incremental scan rates from 1 to 5 mV s^{-1} (Fig. S10a–c†) was performed to investigate the Li-ion diffusion behavior. The linear relationships between the specific peak current and square root of scan rates ($v^{0.5}$) for different redox peaks are shown in Fig. 3g and S10d–f.† It is
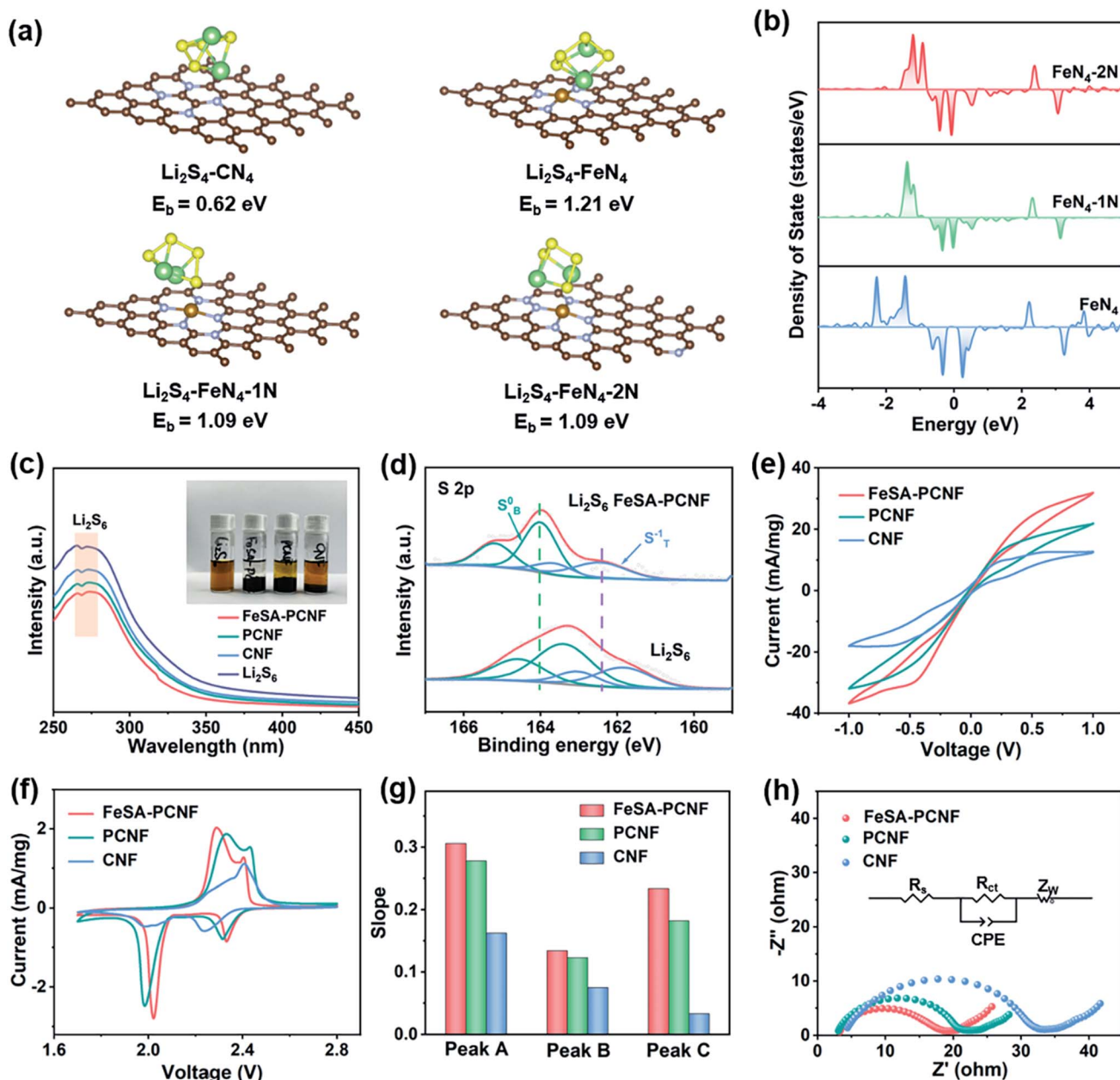
This journal is © The Royal Society of Chemistry 2022

J. Mater. Chem. A, 2022, **10**, 19893–19902 | **19897**

Fig. 3 (a) Optimized binding geometric structures and adsorption energies of Li_2S_4 on different surfaces. (b) Fe 3d DOS profiles of FeN_4, FeN_4-1N and FeN_4-2N. (c) UV-vis spectra and optical images (inset) of LiPSs before and after adsorption by FeSA-PCNF, PCNF, and CNF. (d) S 2p XPS spectra of Li_2S_6 and Li_2S_6 FeSA-PCNF. (e) CV curves of symmetric cells at a scan rate of 1 mV s^{-1}. (f) CV curves of different cathodes at 1 mV s^{-1}. (g) Slopes of peak currents *versus* the square root of scan rates for cathodes measured with scan rates ranging from 1 to 5 mV s^{-1}. (h) EIS curves of different host materials along with the corresponding equivalent circuits.

apparent that FeSA-PCNF demonstrate the highest slopes of all the cathodic and anodic peaks compared to PCNF and CNF, confirming the fastest Li-ion diffusion rate over the entire redox reaction process. The enhanced ion diffusivity should profit from the preferable electrolyte infiltration in the mesoporous and macroporous fiber networks. Fig. 3h shows the Nyquist plot of electrochemical impedance spectroscopy (EIS) for different host materials. Detailed fitting equivalent circuit modeling was also implemented (inset of Fig. 3h). Note that R_s and Z_w represent the resistance of the electrolyte and Warburg element,

respectively. The results demonstrate that the semicircle diameter of the FeSA-PCNF is significantly smaller than that of the PCNF and CNF, indicating a lower charge transfer impedance of FeSA-PCNF by introducing single Fe sites into the porous nanofibers.[36,37]

To demonstrate the practical advantage of FeSA-PCNF in Li–S batteries, CR2032 coin cells were assembled directly using the self-standing fibrous membrane cathodes with FeSA-PCNF and the Li_2S_6-contained electrolyte as the catholyte (see details in the Experimental section in the ESI†). The rate performances of

19898 | *J. Mater. Chem. A*, 2022, **10**, 19893–19902

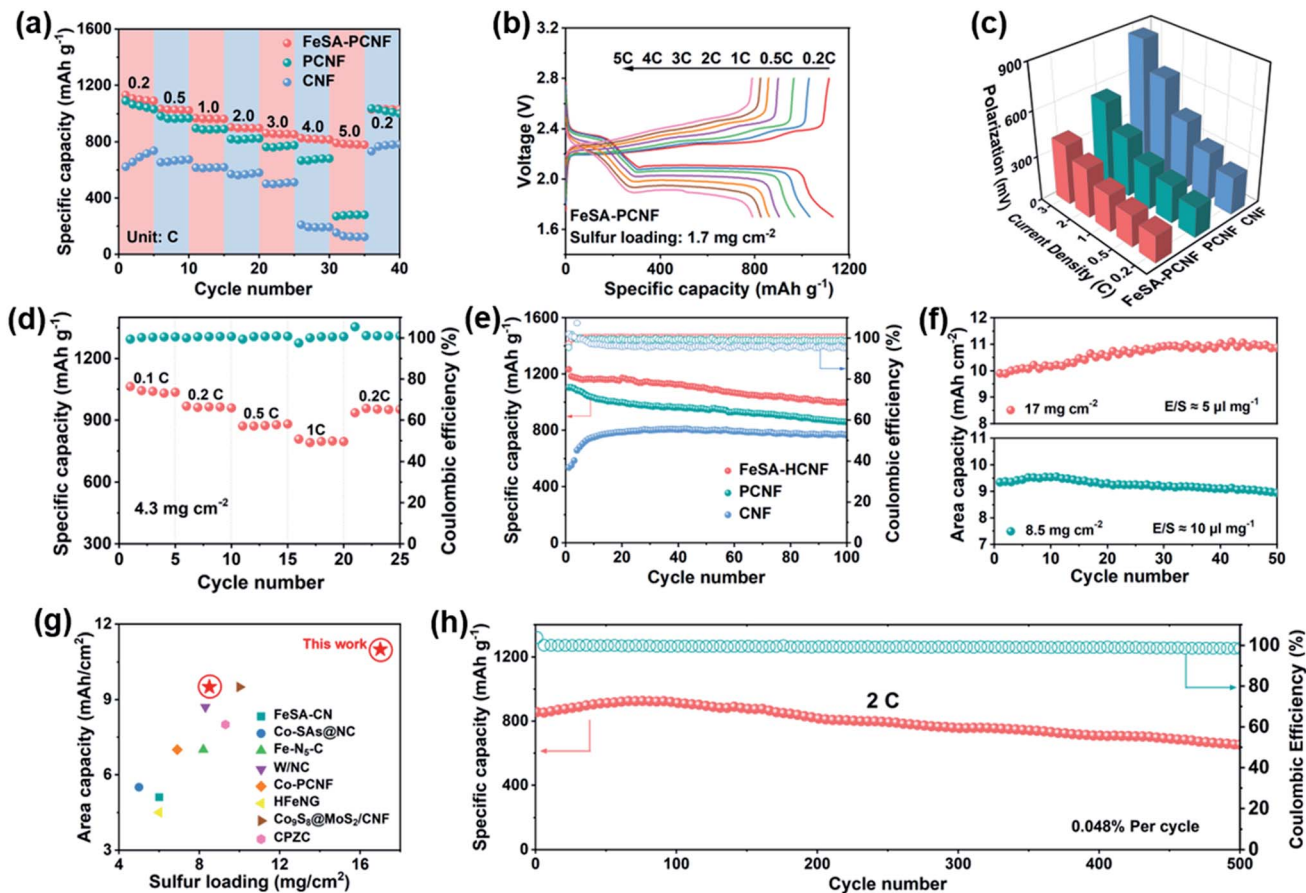This journal is © The Royal Society of Chemistry 2022

Fig. 4 (a) Rate performances of Li−S batteries assembled with FeSA-PCNF, PCNF, and CNF cathodes. (b) Galvanostatic charge−discharge profiles of the FeSA-PCNF cathode at different rates. (c) Voltage polarization of different cathodes at different current rates. (d) Rate performance of the FeSA-PCNF cathode at a sulfur loading of 4.3 mg cm^{-2}. (e) Cycling performances of different cathodes with a sulfur loading of 1.7 mg cm^{-2} at 0.2C. (f) High loading performances with a sulfur loading of 8.5 and 17 mg cm^{-2} at 0.1C. (g) Comparison of the area capacity among this work and reported sulfur cathodes. (h) Long-term cycling performance of the FeSA-PCNF cathode at 2C.

FeSA-PCNF, PCNF, and CNF cathodes at varied current rates from 0.2 to 5C are compared in Fig. 4a. It is apparent that the capacity values of FeSA-PCNF are highest among the investigated cathodes. Even at a high current rate of 5C, a highly reversible capacity of 791 mA h g^{-1} is still retained for FeSA-PCNF, strongly implying the rapid charge transfer rate and high LiPS conversion kinetics. The corresponding discharge/charge voltage profiles (Fig. 4b and S8†) present two discharge plateaus at 2.3 and 2.1 V, referring to the formation of long-chain LiPSs (Li$_2$S$_x$, $4 \leq x \leq 8$) and short-chain lithium sulfides (Li$_2$S$_2$ and Li$_2$S), respectively. The voltage polarization between the charge and discharge profiles of FeSA-PCNF is not obvious and the conspicuous two-step discharge plateau is still detected even at a high rate of 5C (Fig. 4c), in sharp contrast to that of PCNF and CNF (Fig. S11†). Moreover, to demonstrate the potential of FeSA-PCNF for practical application of Li−S batteries, rate performance of FeSA-PCNF with a high sulfur loading of 4.3 mg cm^{-2} was also evaluated (Fig. 4d). Remarkably, a reversible capacity of 758 mA h g^{-1} is achieved at 1C, which is increased to 923 mA h g^{-1} after the current returns to 0.2C. The excellent rate performances of FeSA-PCNF are on

account of the unique porous and long-range ordered carbon nanofiber structures as well as the high electrocatalytic activity of single Fe sites of FeSA-PCNF.

Furthermore, the cycling performances of different cathodes are compared at a current rate of 0.2C (Fig. 4e and S12†). FeSA-PCNF deliver the highest initial specific capacity of 1183 mA h g^{-1}, which is retained at 998 mA h g^{-1} after 100 cycles. It is worth noting that the discharge capacity of CNF increases obviously in the first few cycles, which should be related to the insufficient porosity and the incomplete infiltration of the catholyte.[19,38] The morphology of different components of the Li−S batteries after 100 cycles was also characterized by SEM. The structures of FeSA-PCNF are maintained well and Li$_2$S is uniformly distributed over the whole nanofibers (Fig. S13†), which indicates the excellent electrocatalytic ability of FeSA-PCNF for the rapid conversion of LiPSs and even precipitation of Li$_2$S. In contrast, for PCNF and CNF, lamellar Li$_2$S is observed in the nanofibers.[39] The vast uneven Li$_2$S could significantly affect the conductivity of cathodes and is difficult to be decomposed during the following charge process. In addition, the color of the corresponding separators

This journal is © The Royal Society of Chemistry 2022

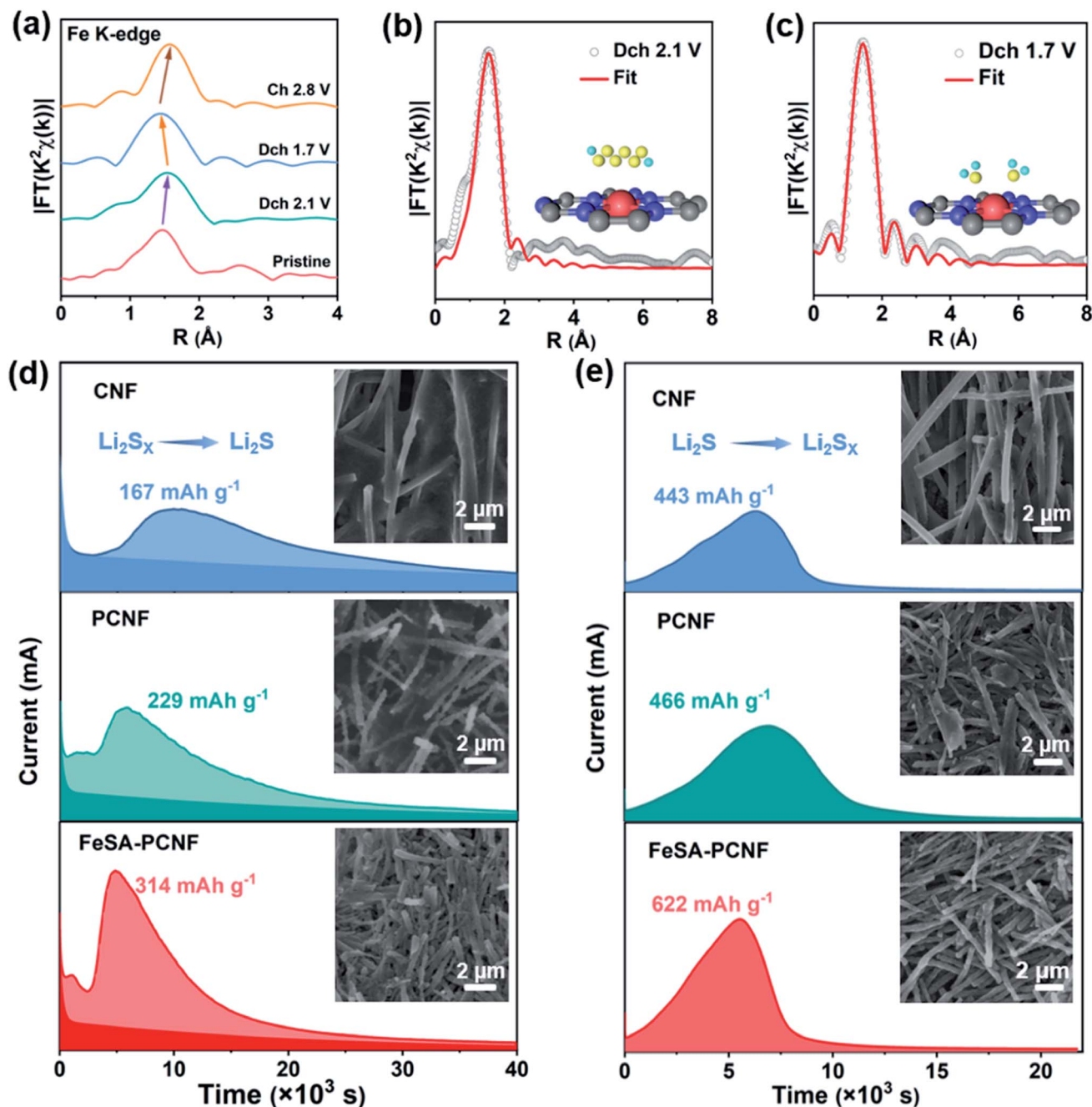*J. Mater. Chem. A*, 2022, **10**, 19893–19902 | **19899**

Fig. 5   (a) Fe K-edge FT-EXAFS spectra of FeSA-PCNF at different states of charge. (b) and (c) The corresponding fitting curves of FeSA-PCNF after discharging to 2.1 V and 1.7 V. (d) and (e) Deposition and dissolution of Li_2S by measuring the potentiostatic discharge and charge profiles at 2.05 and 2.35 V, respectively.

also indicates the least LiPS dissolution in the electrolyte for FeSA-PCNF (inset of Fig. S13†). It has been reported that the dissolution of LiPSs could also influence the Li metal anodes.[40] Obviously, the Li metal coupled with FeSA-PCNF shows a relatively smoother and more compact surface compared with that coupled with PCNF and CNF (Fig. S15†). Additionally, the long-term cycling stability of FeSA-PCNF was tested (Fig. 4h). Even at a high rate of 2C, it still delivers a high initial capacity of 856 mA h g^{-1}, which is retained at 654 mA h g^{-1} after 500 cycles, corresponding to a low capacity decay rate of 0.048% per cycle.

All these results substantiate that FeSA-PCNF could effectively restrain the shuttle effect and electrocatalytically accelerate LiPS redox kinetics, leading to improved battery durability.

High sulfur loading with a low E/S ratio is critical for achieving practical Li–S batteries with high areal capacity and energy density. As shown in Fig. 4f and S15,† FeSA-PCNF with a high sulfur loading of 8.5 mg cm^{-2} and an E/S ratio of 10 μl mg^{-1} demonstrate a high areal capacity up to 9.8 mA h cm^{-2} and excellent stability over 50 cycles. Even with an ultrahigh sulfur loading of 17 mg cm^{-2} and a low E/S ratio of 5 μl mg^{-1},

the battery can achieve a high areal capacity of 11.1 mA h cm^{-2} (corresponding to a cathode-level volumetric energy density of 1649 W h L^{-1}), which is maintained at 10.7 mA h cm^{-2} after 50 cycles. The advanced electrochemical performances of the FeSA-PCNF cathode are competitive with previously reported high loading sulfur cathodes (Fig. 4g and Table S4†), suggesting the superiority of combining SACs with electrospinning for practical Li–S batteries.

To further investigate the structural evolution of FeSA-PCNF during cycling, Fe K-edge FT-EXAFS characterization of FeSA-PCNF at different states of charge was performed (Fig. 5a). After discharge to 2.1 V, the length of the Fe–N bond increases from 1.47 Å to 1.53 Å. The fitting result suggests that one more Fe–S bond is formed in addition to the initial Fe–N bonds due to the adsorption of LiPSs on single Fe sites (Fig. 5b and Table S3†). With further discharge to 1.7 V, the bond length becomes shorter and no Fe–S bond is observed in the fitting result (Fig. 5c and Table S3†) considering the fact that the formed Li$_2$S is an ionic crystal.[41] When charging back to 2.8 V, the bond length increased and the Fe–S bond is reformed (Fig. S16†). The reversible variation of the bond length implies the reversibility of structure change during the cycling process, highlighting the outstanding structural stability of FeSA-PCNF.

Lastly, the deposition and dissolution measurements of Li$_2$S were performed to corroborate the enhanced liquid–solid and solid–liquid conversions by FeSA-PCNF. The Li$_2$S deposition measurements (Fig. 5d) show that FeSA-PCNF deliver the highest Li$_2$S deposition capacity of 314 mA h g^{-1} compared to that of PCNF (229 mA h g^{-1}) and CNF (167 mA h g^{-1}), suggesting effective Li$_2$S precipitation induced by FeSA-PCNF. In addition, the earliest peak time and the highest peak current with respect to Li$_2$S nucleation on FeSA-PCNF (Fig. S17a†) also affirm the promoted LiPS conversion by single Fe sites. The morphology of nucleated Li$_2$S on different surfaces was further characterized by SEM. As shown in Fig. 5d and S18,† Li$_2$S can be uniformly deposited on the surface of FeSA-PCNF while a large amount of Li$_2$S is deposited at the junction of nanofibers in PCNF and CNF. Such uneven deposition of insulating Li$_2$S will greatly reduce the cathode conductivity and lead to deactivation during the following charging process, as also confirmed in the Li$_2$S dissolution measurement. As shown in Fig. 5e and S17b,† FeSA-PCNF exhibit the highest Li$_2$S decomposition capacity of 622 mA h g^{-1} with an earlier peak time and higher peak current compared with that of PCNF and CNF. The SEM images (Fig. 5e and S19†) also indicate an improved Li$_2$S oxidation process with less Li$_2$S left on the surface of FeSA-PCNF. These results reveal the great potential of FeSA-PCNF for practical application of Li–S batteries, which can provide strong LiPS affinity as well as high electrocatalytic activity to speed up the LiPS redox kinetics.

Conclusions

In summary, we have elaborately designed and synthesized FeSA-PCNF which possess a series of structural and electrocatalytic advantages through electrospinning to construct self-standing and binder-free sulfur cathodes for Li–S batteries. The interconnected fibrous networks coupled with hierarchical porous structures of FeSA-PCNF deliver excellent long-range electron conductivity, efficient ion transportation and abundant active interfaces for LiPS conversion. Fully exposed single Fe sites and numerous N dopants in the carbon matrix can effectively anchor LiPSs to inhibit the shuttle effect. In addition, the electrocatalytic activity of FeN$_4$ moieties is further improved by the surrounding graphitic N atoms incorporated into porous nanofibers, leading to the rapid redox kinetics of LiPSs. Because of these advantages, the Li–S batteries assembled with FeSA-PCNF cathodes demonstrate superior rate performances of 791 mA h g^{-1} at 5C and cycling stability with a low capacity decay rate of 0.048% per cycle over 500 cycles at 2C. Moreover, even at an ultrahigh sulfur loading of 17 mg cm^{-2} and a lean E/S ratio of 5 µl mg^{-1}, a high areal capacity of 11.1 mA h cm^{-2} is retained after 50 cycles, suggesting the practical application of FeSA-PCNF for Li–S batteries. Our present work presents a promising strategy for rationally designing self-standing and binder-free cathodes with strong LiPS immobilization and high electrocatalytic activity to achieve high-energy-density and long-lifespan Li–S batteries.

Author contributions

Gang Zhao and Qiujie Chen: conceptualization, methodology, investigation, formal analysis, writing-original draft, writing-review & editing; Lei Wang: methodology, investigation, formal analysis; Tianran Yan: methodology, investigation; Hongtai Li: methodology, writing-review & editing; Cheng Yuan: methodology, writing-review & editing; Jing Mao: investigation; Xuefei Feng: investigation; Dan Sun and Liang Zhang: conceptualization, supervision, project administration, funding acquisition, writing-original draft, writing-review & editing.

Conflicts of interest

There are no conflicts to declare.

Acknowledgements

References

1 P. G. Bruce, S. A. Freunberger, L. J. Hardwick and J.-M. Tarascon, *Nat. Mater.*, 2011, **11**, 172.
2 Y. Cao, M. Li, J. Lu, J. Liu and K. Amine, *Nat. Nanotechnol.*, 2019, **14**, 200–207.

This journal is © The Royal Society of Chemistry 2022

J. Mater. Chem. A, 2022, **10**, 19893–19902 | **19901**

3 A. Manthiram, S. H. Chung and C. Zu, *Adv. Mater.*, 2015, **27**, 1980–2006.

4 A. Manthiram, Y. Fu, S. H. Chung, C. Zu and Y. S. Su, *Chem. Rev.*, 2014, **114**, 11751–11787.

5 Y. Song, W. Cai, L. Kong, J. Cai, Q. Zhang and J. Sun, *Adv. Energy Mater.*, 2019, **10**, 1901075.

6 P. Wang, B. Xi, M. Huang, W. Chen, J. Feng and S. Xiong, *Adv. Energy Mater.*, 2021, **11**, 2002893.

7 T. Meng, J. Gao, J. Zhu, N. Li, M. Xu, C. M. Li and J. Jiang, *J. Mater. Chem. A*, 2020, **8**, 11976–11985.

8 Y. Yan, H. Li, C. Cheng, T. Yan, W. Gao, J. Mao, K. Dai and L. Zhang, *J. Energy Chem.*, 2021, **61**, 336–346.

9 G. Liu, C. Yuan, P. Zeng, C. Cheng, T. Yan, K. Dai, J. Mao and L. Zhang, *J. Energy Chem.*, 2022, **67**, 73–81.

10 Q. Li, M. Liu, X. Qin, J. Wu, W. Han, G. Liang, D. Zhou, Y.-B. He, B. Li and F. Kang, *J. Mater. Chem. A*, 2016, **4**, 12973–12980.

11 C. Yuan, P. Zeng, C. Cheng, T. Yan, G. Liu, W. Wang, J. Hu, X. Li, J. Zhu and L. Zhang, *CCS Chem.*, 2021, **3**, 2826–2838.

12 P. Zeng, C. Liu, X. Zhao, C. Yuan, Y. Chen, H. Lin and L. Zhang, *ACS Nano*, 2020, **14**, 11558–11569.

13 Z. Gu, C. Cheng, T. Yan, G. Liu, J. Jiang, J. Mao, K. Dai, J. Li, J. Wu and L. Zhang, *Nano Energy*, 2021, **86**, 106111.

14 Q. Pang, X. Liang, C. Y. Kwok, J. Kulisch and L. F. Nazar, *Adv. Energy Mater.*, 2016, **7**, 1601630.

15 T. Liu, H. Hu, X. Ding, H. Yuan, C. Jin, J. Nai, Y. Liu, Y. Wang, Y. Wan and X. Tao, *Energy Storage Mater.*, 2020, **30**, 346–366.

16 Y. Hu, W. Chen, T. Lei, Y. Jiao, J. Huang, A. Hu, C. Gong, C. Yan, X. Wang and J. Xiong, *Adv. Energy Mater.*, 2020, **10**, 200082.

17 M. Liu, N. Deng, J. Ju, L. Fan, L. Wang, Z. Li, H. Zhao, G. Yang, W. Kang, J. Yan and B. Cheng, *Adv. Funct. Mater.*, 2019, **29**, 1905467.

18 G. Li, W. Lei, D. Luo, Y. Deng, Z. Deng, D. Wang, A. Yu and Z. Chen, *Energy Environ. Sci.*, 2018, **11**, 2372–2381.

19 R. Saroha and J. S. Cho, *Small Methods*, 2022, e2200049.

20 J. Zhang, Z. Li and X. W. Lou, *Angew. Chem., Int. Ed.*, 2017, **56**, 14107–14112.

21 Z. Li, J. Zhang, Y. Lu and X. W. Lou, *Sci. Adv.*, 2018, **4**, eaat1687.

22 T. Huang, Y. Sun, J. Wu, J. Jin, C. Wei, Z. Shi, M. Wang, J. Cai, X. T. An, P. Wang, C. Su, Y. Y. Li and J. Sun, *ACS Nano*, 2021, **15**, 14105–14115.

23 R. Xiao, K. Chen, X. Zhang, Z. Yang, G. Hu, Z. Sun, H.-M. Cheng and F. Li, *J. Energy Chem.*, 2021, **54**, 452–466.

24 C. Wang, H. Song, C. Yu, Z. Ullah, Z. Guan, R. Chu, Y. Zhang, L. Zhao, Q. Li and L. Liu, *J. Mater. Chem. A*, 2020, **8**, 3421–3430.

25 Y. Zhang, J. Liu, J. Wang, Y. Zhao, D. Luo, A. Yu, X. Wang and Z. Chen, *Angew. Chem., Int. Ed.*, 2021, **60**, 26622–26629.

26 J. Wang, W. Qiu, G. Li, J. Liu, D. Luo, Y. Zhang, Y. Zhao, G. Zhou, L. Shui, X. Wang and Z. Chen, *Energy Storage Mater.*, 2022, **46**, 269–277.

27 Y. He, H. Guo, S. Hwang, X. Yang, Z. He, J. Braaten, S. Karakalos, W. Shan, M. Wang, H. Zhou, Z. Feng, K. L. More, G. Wang, D. Su, D. A. Cullen, L. Fei, S. Litster and G. Wu, *Adv. Mater.*, 2020, **32**, e2003577.

28 Y. Kong, Y. Li, X. Sang, B. Yang, Z. Li, S. Zheng, Q. Zhang, S. Yao, X. Yang, L. Lei, S. Zhou, G. Wu and Y. Hou, *Adv. Mater.*, 2022, **34**, e2103548.

29 H. Zhang, S. Hwang, M. Wang, Z. Feng, S. Karakalos, L. Luo, Z. Qiao, X. Xie, C. Wang, D. Su, Y. Shao and G. Wu, *J. Am. Chem. Soc.*, 2017, **139**, 14143–14149.

30 B. Zhang, X. Qin, G. R. Li and X. P. Gao, *Energy Environ. Sci.*, 2010, **3**, 1531–1537.

31 G. M. Zhou, E. Paek, G. S. Hwang and A. Manthiram, *Nat. Commun.*, 2015, **6**, 7760.

32 Y. Chen, S. Ji, Y. Wang, J. Dong, W. Chen, Z. Li, R. Shen, L. Zheng, Z. Zhuang, D. Wang and Y. Li, *Angew. Chem., Int. Ed.*, 2017, **56**, 6937–6941.

33 D. Xia, D. Yang, L. Xie, Y. Wei, W. Jiang, M. Dou, X. Li, J. Li, L. Gan and F. Kang, *Adv. Funct. Mater.*, 2019, **29**, 1906174.

34 S. Zhang, X. Ao, J. Huang, B. Wei, Y. Zhai, D. Zhai, W. Deng, C. Su, D. Wang and Y. Li, *Nano Lett.*, 2021, **21**, 9691–9698.

35 J. Liu, H. Li, J. Wang, Y. Zhang, D. Luo, Y. Zhao, Y. Li, A. Yu, X. Wang and Z. Chen, *Adv. Energy Mater.*, 2021, **11**, 2101926.

36 W. Yao, W. Zheng, K. Han and S. Xiao, *J. Mater. Chem. A*, 2020, **8**, 19028–19042.

37 J. Jin, W. Cai, J. Cai, Y. Shao, Y. Song, Z. Xia, Q. Zhang and J. Sun, *J. Mater. Chem. A*, 2020, **8**, 3027–3034.

38 K. Sun, H. Liu and H. Gan, *J. Electrochem. Energy Convers. Storage*, 2016, **13**, 021002.

39 J. H. Yun, J. H. Kim, D. K. Kim and H. W. Lee, *Nano Lett.*, 2018, **18**, 475–481.

40 B. Li, Q. Su, L. Yu, J. Zhang, G. Du, D. Wang, D. Han, M. Zhang, S. Ding and B. Xu, *ACS Nano*, 2020, **14**, 17285–17294.

41 L. Zhang, D. Sun, J. Feng, E. J. Cairns and J. Guo, *Nano Lett.*, 2017, **17**, 5084–5091.

19902 | *J. Mater. Chem. A*, 2022, **10**, 19893–19902

This journal is © The Royal Society of Chemistry 2022